Architecting "Li-rich Ni-rich" core-shell layered cathodes for high-energy Li-ion batteries

Zhiwei Jing [a,1], Suning Wang [a,b,1], Qiang Fu [b], Volodymyr Baran [c], Akhil Tayal [c], Nicola P.M. Casati [d], Alexander Missyul [e], Laura Simonelli [e], Michael Knapp [b], Fujun Li [f], Helmut Ehrenberg [b], Sylvio Indris [b], Chongxin Shan [g], Weibo Hua [a,b,f,*]

[a] School of Chemical Engineering and Technology, Xi'an Jiaotong University, No.28, West Xianning Road, Xi'an, Shaanxi 710049, China
[b] Institute for Applied Materials (IAM), Karlsruhe Institute of Technology (KIT), Hermann-von-Helmholtz-Platz 1, Eggenstein-Leopoldshafen D-76344, Germany
[c] Deutsches Elektronen-Synchrotron (DESY), Notkestr. 85, Hamburg 22607, Germany
[d] Paul Scherrer Institut (PSI), WLGA/229, Villigen PSI 5232, Switzerland
[e] CELLS-ALBA Synchrotron, Cerdanyola del Valles, Barcelona E-08290 Spain
[f] Key Laboratory of Advanced Energy Materials Chemistry (Ministry of Education), College of Chemistry, Nankai University, Tianjin 300071, China
[g] Key Laboratory of Materials Physics of Ministry of Education, School of Physics and Microelectronics, Zhengzhou University, Daxue Road 75, Zhengzhou 450052 China

Keywords:
Ni-rich cathodes
Li-rich cathodes
Core-shell architecture
Interdiffusion
Cycling stability

A B S T R A C T

Li-rich or Ni-rich layered oxides are considered ideal cathode materials for high-energy Li-ion batteries (LIBs) owing to their high capacity (> 200 mAh g^{-1}) and low cost. However, both are suffering from severe structural instability upon high-voltage cycling (> 4.5 V). Here, "Li-rich Ni-rich" $Li_{1.08}Ni_{0.9}Mn_{0.1}O_2$ oxides with core-shell architecture are designed and synthesized to improve their high-voltage cyclability. These oxides are determined to be composed of a less reactive "Li-rich Mn-rich" shell and a high-capacity "Li-rich Ni-rich" core. As Li-ions gradually enter into the core-shell precursor during high-temperature lithiation reaction, the interdiffusion of elements across the interphase between the Mn-rich shell and the Ni-rich core successively occurs. Such thermally-driven atomic interdiffusion could lead to a thickness-controllable "Li-rich Mn-rich" shell, which can guarantee an exceptional structural reversibility for the layered "Li-rich Ni-rich" core upon long-term cycling. As a consequence, the optimized core-shell $Li_{1.08}Ni_{0.9}Mn_{0.1}O_2$ achieves a capacity retention of 96% at 0.1 C after 100 cycles in the voltage range of 2.7–4.6 V. These findings might open up a new avenue for rational design of advanced cathode materials for LIBs and beyond.

1. Introduction

In recent years lithium-ion batteries (LIBs) have been extensively applied in various applications, such as portable electronics for the fourth industrial revolution, electric vehicles (EVs) and large-scale energy storage systems [1–4]. Achieving the climate goals of the Paris Agreement is driving the growing requirements of LIBs, and the estimated scale of required LIBs will reach TWh scales by 2030 [5–10]. This has led to global research efforts toward advanced LIBs with higher energy density and longer lifetime [11]. Currently, layered Li(Ni,Co,Mn)O_2 (NCM, space group $R\bar{3}m$) cathode materials are particularly attractive because of their high volumetric and gravimetric energy densities [12,13]. The specific energy (E_S) of NCM is determined by the average discharge potential (V) and the specific capacity (C) (i.e. $E_S = \int V(C)dC$) [14,15]. Thus, Ni-rich layered $Li(Ni_xCo_yMn_{1-x-y})O_2$ ($x \geq 0.6$) compounds are regarded as one of the most promising cathode materials for EV batteries because their higher amount of the $Ni^{2+}/Ni^{3+}/Ni^{4+}$ redox couple could enable EVs to achieve a higher mileage per charge [2, 16–20].

Normally, the delivered reversible capacity of Ni-rich NCM cathodes is approximately 200 mAh g^{-1} when the LIBs are charged to 4.3 V, which is still lower than their theoretical capacity (around 280 mAh g^{-1}) [21, 22]. Making a higher energy density of Ni-rich cathodes viable requires deintercalation/intercalation of a larger number of Li-ions and electrons from/into the layered structure ($R\bar{3}m$) by an increased potential window [23,24]. Unfortunately, a large amount of highly reactive Ni^{4+} species

* Corresponding author at: School of Chemical Engineering and Technology, Xi'an Jiaotong University, No.28, West Xianning Road, Xi'an, Shaanxi 710049, China.
E-mail address: weibo.hua@xjtu.edu.cn (W. Hua).
[1] These authors contributed equally to this work.

would be generated at the surface of the particles when charged to higher potentials (> 4.2 V) [25–27], which causes parasitic side reactions such as oxygen release [24] and surface reconstruction from layered to spinel or rock-salt structure [28], etc., and thus results in the deterioration of electrochemical performances. Controllable synthesis of secondary particles with a Mn-rich shell surrounding a Ni-rich core or a transition-metal (TM) concentration gradient is found to be an efficacious approach to improve the chemical and structural stability of Ni-rich cathodes [29–31]. However, the Mn ions in the shell-phase are prone to diffuse to the core during the high-temperature lithiation process (≥ 700 °C) making the surface passivation less effective [32,33]. On the other hand, Li- and Mn-rich layered cathode materials can deliver exceptionally high capacity (>250 mA h g ^{1}) stemming from both cationic and anionic redox reactions, but these materials are plagued by severe voltage decay upon cycling [7,34,35]. Recently, Tarascon's group [36] and Ma's group [37] proposed a new concept of "Li-rich Ni-rich" layered oxide cathode materials, which could exhibit an improved cycling stability and a robust oxygen lattice structure framework. Nevertheless, few studies have focused on the controllable synthesis of "Li-rich Ni-rich" layered oxides with a core-shell architecture.

Herein, a core-shell-architectured $Ni(OH)_2$@$Mn(OH)_2$ precursor was prepared by a precipitation method. The cation interdiffusion and structural evolution during the synthesis of "Li-rich Ni-rich" core-shell $Li_{1.08}Ni_{0.9}Mn_{0.1}O_2$ oxides were carefully analysed and characterized by a combination of analytical methods. As the heating temperature increases to about 700 °C, the mixture of the core-shell precursor and LiOH•H_2O gradually converts to a compound with a layered "Li-rich Ni-rich" core ($R\bar{3}m$) and a monoclinic layered "Li-rich Mn-rich" shell ($C2/m$) on a secondary particle level. Both layered phases would convert into a single-layered $Li_{1.08}Ni_{0.9}Mn_{0.1}O_2$ phase ($R\bar{3}m$) completely with a further increase of temperature above 800 °C, driven by the concentration gradient of Ni/Mn ions. It is evident that a thin layer of less reactive Li- and Mn-rich phase on the top of a Ni-rich primary particle can be formed at an appropriate temperature (e.g. 750 °C), which is favorable for improving cycling stability. The enhanced structural stability of Ni-rich core-shell cathode materials was further supported by in situ high-resolution synchrotron-based X-ray diffraction (SXRD). This study provides new insights into the cation interdiffusion during thermal treatment and an effective approach for alleviating structural fatigue upon high-voltage cycling.

2. Results and discussion

To synthesize the core-shell-architectured $Ni(OH)_2$@$Mn(OH)_2$

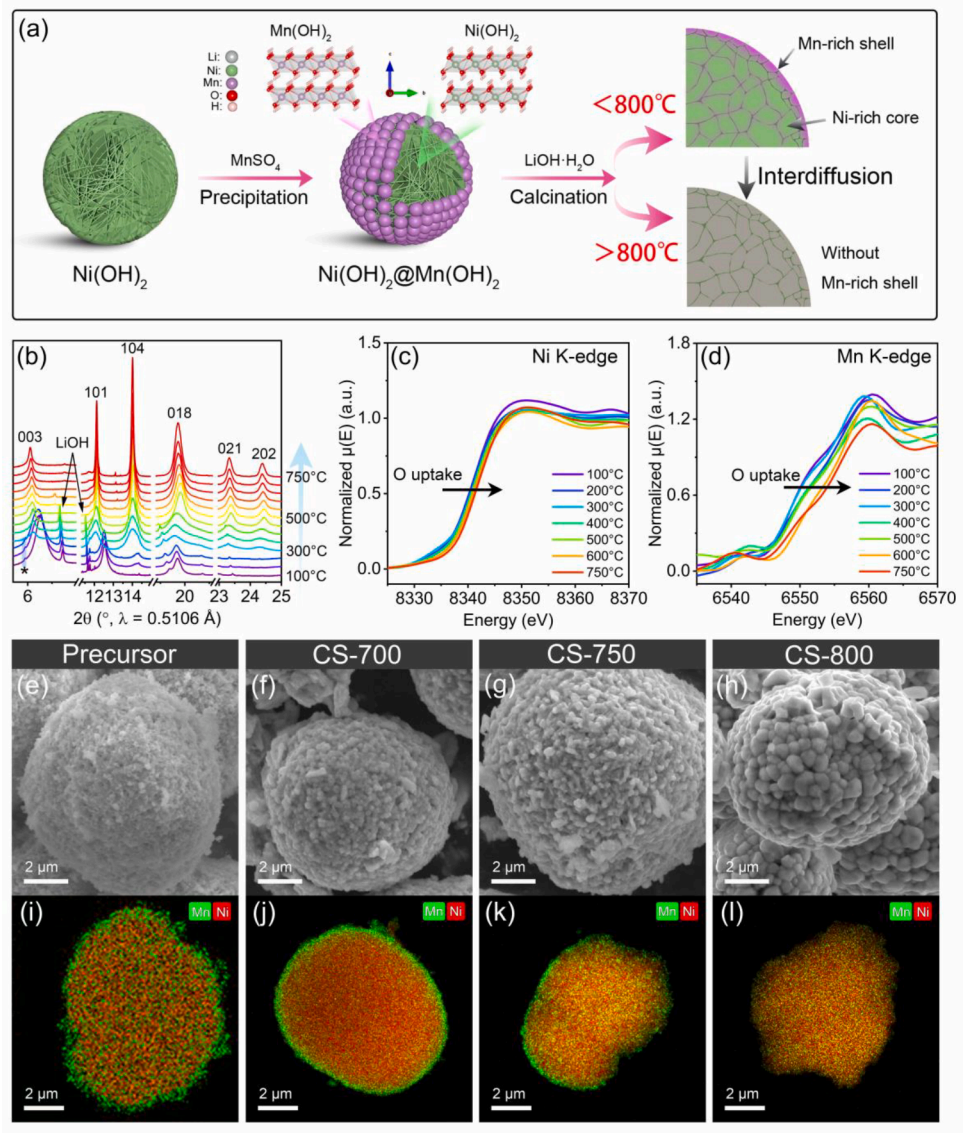

Fig. 1. Structural evolution and cation interdiffusion during synthesis of core-shell layered $Li_{1.08}Ni_{0.9}Mn_{0.1}O_2$. (a) Schematic illustration for the formation and disappearance of the core-shell architecture; (b) in situ HT-SXRD patterns of a mixture of core-shell Ni$(OH)_2$@$Mn(OH)_2$ precursor and LiOH from 100 °C to 750 °C, the asterisk denotes Mn_3O_4; in situ XANES spectra at (c) Ni and (d) Mn K-edges for the reactants during heating; SEM images of (e) $Ni(OH)_2$@$Mn(OH)_2$, (f) CS-700, (g) CS-750 and (f) CS-800, and (i-l) their corresponding TEM-EDX elemental maps.

precursor, layered $Ni(OH)_2$ ($P\bar{3}m1$) was firstly prepared via a precipitation method [38,39] (see Figs. 1a and S1, supporting information). A $NiSO_4{\cdot}6H_2O$ aqueous solution, a NaOH solution (aq.) and a desired amount of NH_4OH solution (aq.) were simultaneously and separately added into a reactor Nr.1. After the nucleation and crystallization processes (20 h), the $Ni(OH)_2$ precipitates were fed into a reactor Nr.2 as crystal nuclei. Subsequently, a $MnSO_4{\cdot}H_2O$ solution, a NaOH solution and an ammine solution were added into the reactor Nr.2, respectively. The molar ratio of $NiSO_4{\cdot}6H_2O$ solution to $MnSO_4{\cdot}H_2O$ solution is 9:1. The resultant powders were filtered, washed and dried for the removal of impurity ions and absorbed H_2O. For comparison, homogeneous $Ni_{0.9}Mn_{0.1}(OH)_2$ was also prepared by a co-precipitation method on the basis of our previous work [12,40,41].

Both $Ni(OH)_2$ and $Ni_{0.9}Mn_{0.1}(OH)_2$ particles are spherical secondary particles composed of thin nanoplates, see Fig. S2. The average size of the $Ni(OH)_2$ and $Ni_{0.9}Mn_{0.1}(OH)_2$ agglomerates is determined to be 12.2 and 9.2 μm, respectively (Fig. S3). There are several nanoparticles on the surface of the $Ni(OH)_2$@$Mn(OH)_2$ precursor (Figs. 1e and Figure S2), resulting in a slight increase in the average secondary-particle size compared with $Ni(OH)_2$ (Figure S3). The $Ni(OH)_2$@$Mn(OH)_2$ agglomerates containing a Mn-rich shell and a Ni-rich core can be observed clearly by both cross sectional scanning electron microscopy coupled with energy dispersive X-ray analysis (SEM-EDX, Figure S4) and transmission electron microscopy combined with EDX maps (TEM-EDX, Figs. 1i–l). The small particle size of the Mn-rich shell is predominantly due to a relatively high solubility-product constant of $Mn(OH)_2$ (log K_{sp}: 12.7) compared to that of $Ni(OH)_2$ (log K_{sp}: 15.2) [42]. All the reflections in the XRD patterns of $Ni(OH)_2$ and $Ni_{0.9}Mn_{0.1}(OH)_2$ can be indexed according to a single-layered CdI_2-type structure ($P3m1$), as shown in Fig. S5. In addition to the main layered phase ($P\bar{3}m1$), a set of weak reflections belonging to a tetragonal spinel Mn_3O_4 ($I4_1/amd$) are found in the XRD pattern of core-shell $Ni(OH)_2$@$Mn(OH)_2$, which is possibly caused by the oxidation of $Mn(OH)_2$ in air.

In situ high-temperature synchrotron-based X-ray diffraction (HT-SXRD) and absorption spectroscopy (HT-XAS) were used to investigate the structural evolution and charge compensation mechanism during the synthesis of core-shell-architectured $Li_{1.08}Ni_{0.9}Mn_{0.1}O_2$, as shown in Figs. 1b–d. At low temperatures (< 300 °C), the main reflections in the in situ HT-SXRD patterns can be assigned to a layered $Ni(OH)_2$ ($P\bar{3}m1$) and a tetragonal LiOH ($P4/nmm$). When the temperature is increased to around 500 °C, the reflections from $Ni(OH)_2$ and LiOH gradually vanish, and a new set of reflections belonging to a rhombohedral layered structure ($R\bar{3}m$) successively appear, which indicate the occurrence of the Li^+/H^+-ion exchange reaction at a relatively low temperature. As the temperature further increases to 750 °C, an increased intensity of 003 reflection suggests a phase transformation from disordered layered ($R\bar{3}m$) to ordered layered phase ($R\bar{3}m$). Generally, the integrated intensity ratio of the 003 reflection to 104 reflection (I_{003}/I_{104}) is higher than 1.2 in the layered structure. [43] The low ratio of I_{003}/I_{104} in the SXRD pattern obtained at 750 °C is due to the limited heating time during the HT-SXRD experiments (< 1 h). The X-ray absorption near-edge structure (XANES) region of the in situ HT-XAS spectra of the reactants is sensitive to the oxidation state and local symmetry of Ni and Mn ions. The normalized Ni K-edge and Mn K-edge XANES spectra are presented in Figs. 1c and d. The valence states of Ni and Mn are estimated to be approximately 2.0+ and 2.5+ at the initial stage of the heating process. Both Ni K-edge and Mn K-edge XANES spectra obviously shift towards higher energy as the high-temperature lithiation reaction proceeds, demonstrating that the valence states of Ni and Mn cations are increased with the insertion of Li-ions. These data reveal that ambient oxygen anions are progressively incorporated into the host structure to maintain electrical neutrality and provide the coordination sites for the inserted Li-ions in the calcination process.

According to the in situ HT-SXRD and HT-XAS results, the temperatures for the lithiation reaction were chosen as 650, 700, 750, 800, and 850 °C for 12 h to prepare the oxides with core-shell (CS) morphology and explore the interdiffusion in detail. The obtained samples were marked as CS-650, CS-700, CS-750, CS-800 and CS-850, respectively. The overall chemical composition of the synthesized core-shell oxides measured by inductively coupled plasma mass spectrometry (ICP-MS, Table S1) shows that their atomic ratios of Li:Ni:Mn is around 1.08 (1):0.90(2):0.10(1), which agrees well with the theoretical value. For comparison, the layered $LiNiO_2$ ($R\bar{3}m$, LNO) obtained at 650, 700, 750, 800, and 850 °C were labelled as LNO-650, LNO-700, LNO-750, LNO-800, and LNO-850. The layered $Li_{1.08}Ni_{0.9}Mn_{0.1}O_2$ ($R\bar{3}m$) with a uniform distribution of TM ions was prepared at 800 °C for 12 h (LNMO-800). The spherical morphology of the secondary particles is basically preserved after the thermal treatment. Obviously, the primary particle size in the near-surface region of both CS and LNO agglomerates increases with increasing temperature, as depicted in Figs. 1f–h and S6. However, the average primary particle diameter of LNO crystallites is larger than that of CS particles at each temperature because of the Mn-rich nanoparticles on the surface of $Ni(OH)_2$@$Mn(OH)_2$ agglomerates. The Ni-rich particle core and Mn-rich shell with a thickness of about 220 nm can evidently be seen from TEM-EDX mapping images of CS-700 (Fig. 1j). The Mn-rich outer surface on the top of the Ni-rich core becomes thinner when the heating temperature is increased from 700 to 750 °C and eventually vanishes at even higher temperatures (≥ 800 °C), see Figs. 1j–l and S6,S7. A decrease in the thickness of the Mn-based shell and a more homogeneous distribution of TM ions with increasing temperature provide direct evidence for an interdiffusion of Ni/Mn ions during annealing driven by concentration gradient.

High-resolution SXRD was utilized to investigate the crystallographic structure of the samples, as shown in Fig. S9. All the reflections in the SXRD patterns of CS samples can be indexed according to a single rhombohedral layered α-$NaFeO_2$ structure ($R\bar{3}m$). With increasing the calcination temperature, the splitting of the two Bragg peaks of 006/102 and 018/110 becomes clear, suggesting an increased lattice distortion of the cubic-close packed (ccp) oxygen framework along the [111] direction and the generation of a better-defined rhombohedral layered structure [44]. Simultaneously, the full width at half maximum (FWHM) of all reflections tends to become narrower, which is consistent with an increase of the crystallite size at higher heating temperatures (see Figs. 1f–h and S6). Rietveld refinements were completed by using a rhombohedral layered structure model $[Li_{1.08-x}Ni_x]_{3a}[Ni_{0.9-x}Li_xMn_{0.1}]_{3b}O_2$ ($R\bar{3}m$). The refinement results, including the calculated lattice parameters (e.g. a and c), unit-cell volume (V) and the degree of Li/Ni cation exchange, are given in Fig. S10 and Table S2 in the Supporting Information, which are in good agreement with previously reported values for Ni-rich layered materials [41,45,46]. Apparently, no obvious secondary phase belonging to the rhombohedral layered structure ($R\bar{3}m$) is observed in CS-650, CS-700 and CS-750, which signifies that the Mn-rich shell phase possesses a very similar layered structure. The normalized Ni K-edge and Mn K-edge XANES spectra of CS oxides (Fig. S11) show that the valence states of Ni and Mn ions are estimated to be +3 and +4, respectively. These results indicate a completion of lithium/oxygen incorporation when the heating temperature is higher than 650 °C.

To further study the thermal annealing induced interdiffusion process, the TEM–EDX mapping measurements were carried out on the outer surface of CS-700, CS-750 and CS-800, respectively. Clearly, there is a Ni-rich layer on the primary particle surface in the Mn-rich shell of a CS-700 agglomerate (see Fig. 2a), which suggests that Ni ions from the inner Ni-rich core had diffused to the near-surface region of secondary particles. Fig. 2c shows a high-resolution TEM (HRTEM) image of CS-700 taken along $[312]_M$ orientation. The Fast Fourier Transform (FFT) patterns in the selected area of Fig. 2c exhibit an array of dots with monoclinic layered symmetry, correlated with the traditional "Li-rich Mn-rich" phase ($C2/m$) [47–50]. The inverse FFT (IFFT)–HRTEM image was filtered using the standard diffraction spot, as shown in Fig. 2d.

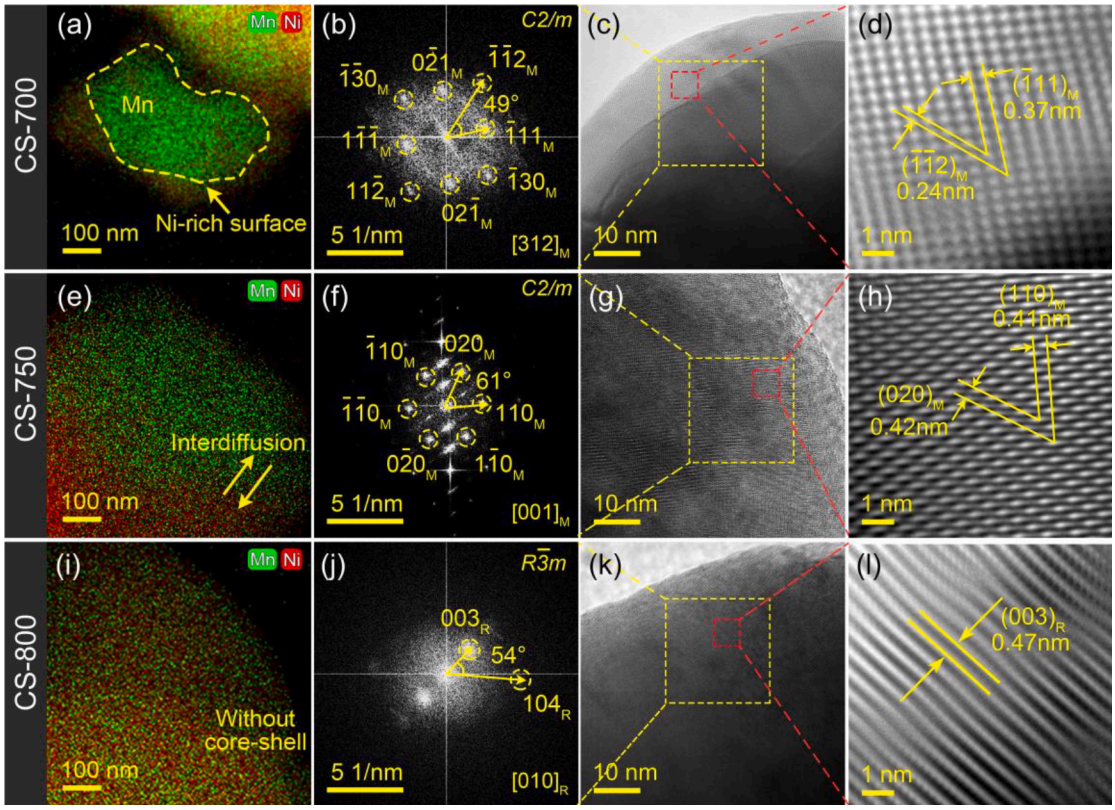

Fig. 2. Changes in the local structure and elemental distribution in the near-surface region of agglomerates at various temperatures. TEM-EDX mapping images of (a) CS-700, (e) CS-750 and (i) CS-800; (c, g, k) HRTEM images, (b, f, j) corresponding selected area FFT patterns and (d, h, l) IFFT-HRTEM images of CS-700, CS-750 and CS-800. Subscript M and R represent the monoclinic (*C2/m*) and rhombohedral ($R\bar{3}m$) layered structures, respectively.

There are two sets of lattice fringes with the interplanar spacing of 0.37 and 0.24 nm at an angle of ≈50°, which can be indexed to the $(11\bar{1})_M$ and $(1\bar{1}\bar{2})_M$ planes of the monoclinic layered structure (*C2/m*). These results are indicative of the formation of a "Li-rich Mn-rich" layered phase with monoclinic, *C2/m* symmetry in the shell of CS-700 (see stage II in Fig. 3) due to the fact that the Li-ions are firstly inserted into the Mn-rich outer surface region of the secondary particles during heating. A relatively large degree of elemental segregation of Ni and Mn can be detected at the outer surface of CS-750, pointing out that the interdiffusion of Ni and Mn ions is gradually enhanced by a successive annealing process (stage III in Fig. 3). The FFT patterns of the selected region in CS-750 exhibit spots for the $(020)_M$, $(110)_M$ and $(1\bar{1}0)_M$ lattice planes (Fig. 2f), which are also consistent with *C2/m* symmetry. The measured lattice fringes in the IFFT-HRTEM image (Fig. 2h) are approximately 0.42 and 0.41 nm, respectively, corresponding to the *d* values of the 020_M and 110_M superstructure reflections of monoclinic "Li-rich Mn-rich" phase. Importantly, the presence of these superstructure reflections manifests the in-plane honeycomb ordering of (Li/Ni)/Mn ions in the *a-b* plane of the monoclinic layered structure, while the typical rhombohedral layered NCM materials do not possess such superstructure reflections. By contrast, a uniform distribution of Ni and Mn ions is probed in CS-800, implying a completion of interdiffusion of TM ions. The HRTEM image (Fig. 2k) and corresponding selected area IFFT image (Fig. 2l) of CS-800 illustrate that the interplanar spacing is around 0.47 nm, which matches precisely with the *d*-spacing of $(003)_R$ crystal plane of the rhombohedral layered structure ($R\bar{3}m$). The corresponding FFT patterns along $[010]_R$ zone axis (Fig. 2j) are in good agreement with $R\bar{3}m$ symmetry. These results reveal that the primary particles in the near-surface region of CS-800 agglomerates possess the same layered rhombohedral structure ($R\bar{3}m$) as the inner core of the secondary particles (see its SXRD pattern in Figure S9, stage IV in Fig. 3).

To understand the correlation between core-shell architecture and electrochemical properties, electrochemical tests were carried out on CR2032-type coin cells at 25 °C. The initial charge-discharge voltage profiles and cycling performances of the electrodes in a narrow voltage range of 2.7 – 4.3 V are shown in Fig. S12. It is clear that CS-750 exhibits an outstanding cycling stability. The capacity retention of CS-750 is nearly 99% at 0.1 C (1 C = 275 mA g^{-1}) after 100 cycles, which is much higher than that of LNMO-800 (76%) and other CS cathodes (CS-650: 93%, CS-700: 95%, CS-800: 62%, CS-850: 46%). On the basis of the instability of Ni-rich cathode materials at higher voltages (> 4.3 V), a wider voltage range (2.7 – 4.6 V) was used to investigate the cyclability of core-shell-architectured Ni-rich cathodes under high-voltage operation, see Figs. 4 and S14. The initial discharge capacities of LNMO-800, CS-700, CS-750 and CS-800 at 0.1 C are 191, 159, 187 and 186 mAh g^{-1}, respectively. A comparatively low capacity of CS-650 and CS-700 is most likely correlated to the higher thickness of the electrochemical inactive "Li-rich Mn-rich" shell. The apparent activation energy (E_a) for the Li-ion extraction from CS-800 (pristine state) is around 0.45 ± 0.02 eV, as exhibited Fig. S15, which is higher than that of CS-750 (0.38 ± 0.02 eV). The higher E_a of CS-800 indicates that the larger primary particle size could impede the Li-ion interfacial transport process, thereby resulting in a low discharge capacity. It can be seen from Figs. 4a–c and S14 that the Co-free Ni-rich cathode materials with core-shell architecture (e.g. CS-700 and CS-750) deliver an outstanding cycling stability during high-voltage cycling. After 100 cycles at 0.1 C, the capacity retention of CS-750 is around 96%, which is higher than that of other cathode materials without core-shell architecture (e.g. LNMO-800: 75% and CS-800: 73%) and superior to most values of Ni-rich cathodes reported in previous literature (see Table S4) [6,36, 51–56]. Except for the improved cyclability, the voltage fading is also effectively suppressed in CS-750 over long-term cycling (see Fig. 4b). The enhanced reversibility in the CS-750 can also be clearly recognized

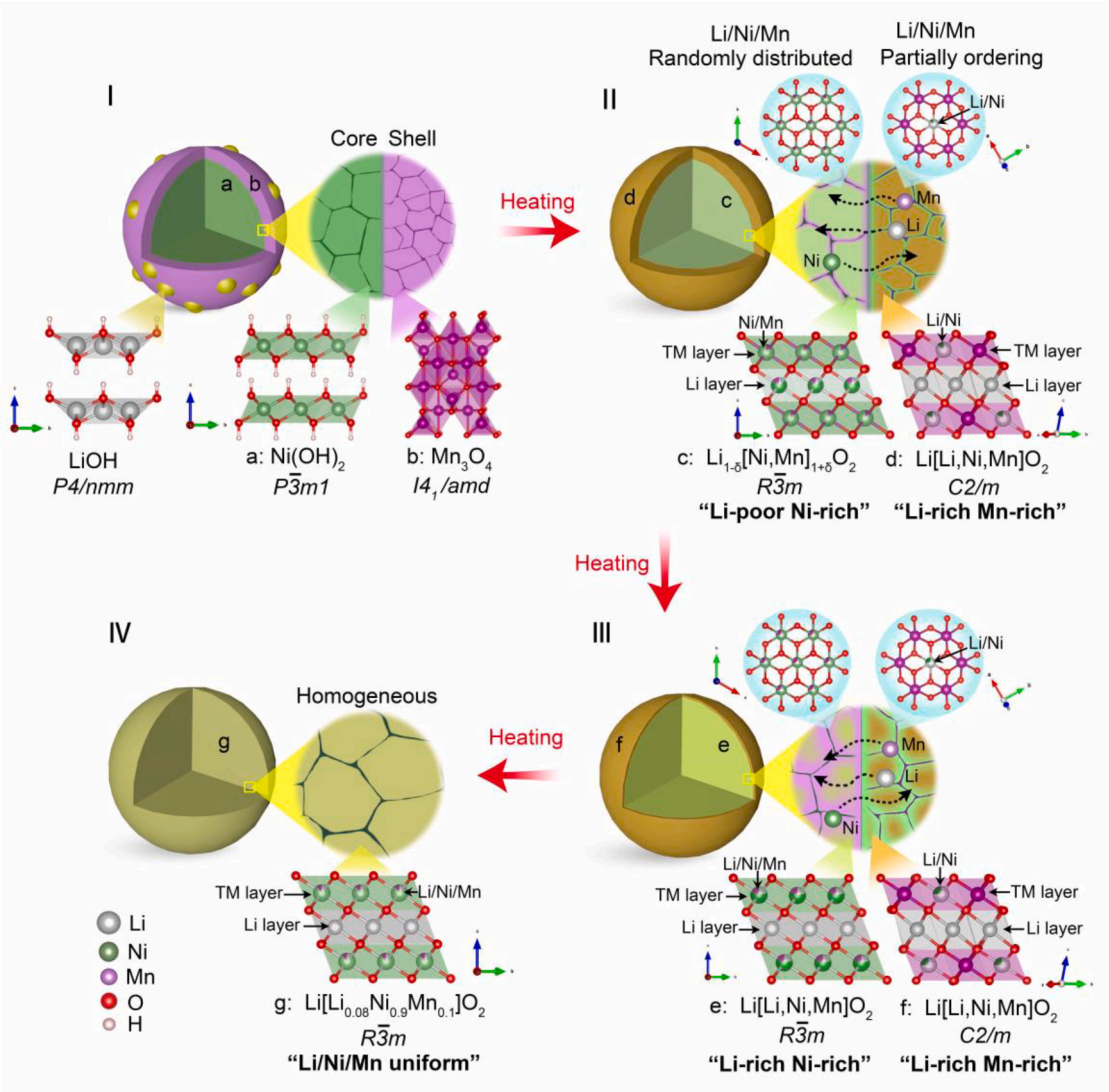

Fig. 3. Schematic illustration for the cation interdiffusion and local structural changes of core-shell-architectured particles.

by the stable oxidation–reduction peaks in the differential capacity versus voltage (dQ/dV) curves upon extended cycling, as illustrated in Figs. 4d–f. The charge-transfer resistances (R_{ct}) of CS-750 and CS-800 in a pristine state are comparable, as exhibited in Fig. S16 and Table S3. The R_{ct} of CS-800 increases from 96 Ω (before cycling) to 1655 Ω after 100 cycles at 0.1 C, which is larger than that of the CS-750 (from 97 to 1141 Ω). The suppression of rapid growth of R_{ct} for CS-750 can be ascribed to the core-shell architecture that could mitigate the lattice distortion during extended cycling (see HRTEM images of fatigued electrodes below). The cycling performances of the prepared cathode materials at a current density of 1 C are displayed in Figs. 4g-h and S18. The capacity retentions of core-shell-architectured CS-700 and CS-750 are higher than those of LNMO-800 and CS-800 after 100 cycles. More excitingly, around 79% and 62% of their initial capacity can still be achieved for and CS-700 and CS-750 after 500 cycles at 1 C. These results are indicative of the outstanding cyclic performance of core-shell architectured cathode materials during high-voltage cycling.

To elucidate the underlying mechanism for the enhanced cyclability of core-shell-architectured cathode materials, in situ SXRD experiments were conducted on CS-750, LNMO-800 and CS-800 cathodes with cycling in the voltage range from 2.7 to 4.6 V (Figs. 5 and S20–S22). No apparent reflection splitting is found in these electrodes, except for a continuous change in reflection positions and intensities during the (de) lithiation process, indicating a quasi-solid-solution reaction, which is in good agreement with reported results [15,16,24]. On the basis of crystallographic theory, the 003, 104 and 018 reflections reflect predominately the change in the lattice parameter c (i.e. the average metal-metal inter-slab distance) of the rhombohedral layered structure ($R\bar{3}m$) [57], whereas the 101 and 110 reflections represent mainly the lattice parameter a or b (the average metal-metal intra-slab distance) of the layered phase [58]. From open-circuit voltage to 4.2 V, the 003, 104, 018 reflections gradually move towards lower 2θ angles, while the 101 and 110 reflections shift towards higher 2θ angles, corresponding to an increased c parameter and a decreased a ($a = b$) parameter. All the reflections move to higher scattering angles in the voltage region from 4.2 to 4.6 V, implying a continuous shrinkage of the unit-cell volume. The contraction of cell volume always occurs at higher voltage regions in conjunction with the formation of severe lattice strain that deteriorates the electrochemical performance of Ni-rich cathode materials (see the discussion below). The lattice parameter variations of three electrodes were obtained from the Rietveld refinement results, as shown in Figs. 5b, d, f. When charged to 4.6 V, the lattice parameter c and the unit-cell volume (V) of the CS-750 cathode change by –1.8 and –5.9% compared to its pristine state, respectively, which are smaller than those of LNMO-800 cathode (–2.6 and –6.7%) and CS-800 cathode (–3.6 and –10.5%). These findings indicate that the core-shell architecture could

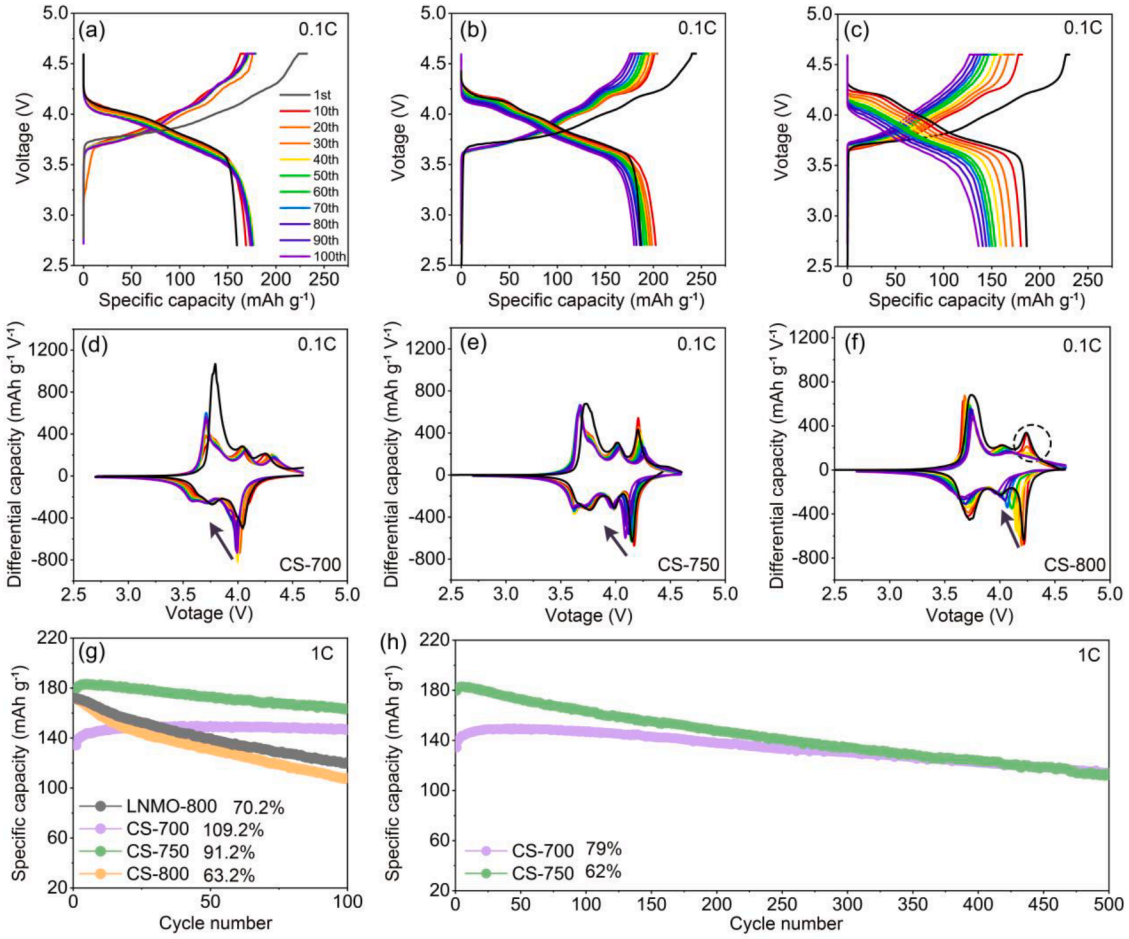

Fig. 4. High-voltage cycling performances of LNMO-800 and CS cathodes between 2.7 and 4.6 V. Charge-discharge voltage profiles of (a) CS-700, (b) CS-750 and (c) CS-800 cathodes from 1st to 100th cycle at 0.1 C between 2.7 and 4.6 V, and (d-f) their corresponding dQ/dV curves; (g) the cyclability of selected cathodes and (h) long-term cycling stability of CS-750 and CS-700 cathodes at 1 C in a voltage range of 2.7 – 4.6 V.

effectively mitigate the structural collapse in *c* direction and the contraction of the layered unit cell. The difference in the unit-cell volume *V* of the CS-750 electrode before and after the first cycle is as low as 0.0735(5) Å^3, which is much lower than that of the LNMO-800 electrode (0.3378(9) Å^3) and CS-800 cathode (0.1432(6) Å^3). Such good reversibility of the CS-750 electrode provides clear evidence that the "Li-rich Mn-rich" shell on top of the Ni-rich core is beneficial for the improvement of the structural stability and cyclic property of Co-free Ni-rich cathodes during high-voltage cycling.

Since the anisotropic lattice contraction and expansion in the layered structure would cause substantial anisotropic microstrains upon the Li^+ insertion/extraction, the anisotropic strain evolutions in [003] and [101] directions were quantitatively analysed (see Figs. 6a and b). As the potential increases to around 4.3 V, the microstrains in CS-750 and LNMO-800 cathodes are gradually accumulated in both (003) and (101) planes. With the voltage further increasing to 4.6 V, a notable rise in the strain evolution along [003] (or [001]) direction can be observed clearly at the highly delithiated state of LNMO-800 cathode, in sharp contrast to a slight increase in the lattice strain of the CS-750 cathode. The microstrain accumulated in the (003) plane of the LNMO-800 cathode at the end of the charge process is approximately 6 times higher than in its pristine state. In contrast, the CS-750 cathode in the highly charged state shows a pronounced suppression of microstrain along [003] direction (see Figs. 6a and g). The lattice strain in the (101) plane in the LNMO-800 cathode firstly increases and subsequently decreases upon charging. The CS-750 cathode exhibits a sluggishness in changing the microstrain along [101] direction upon de-lithiation, further proving its enhanced structural stability. A severe lattice distortion in the near-surface region of LNMO-800 particles along [003] direction is clearly visible when charged to 4.6 V, as evidenced by the HRTEM images in Figs. 6e and f. By contrast, no obvious lattice distortion is detected at the surface of the CS-750 cathode in the (003) plane (Figs. 6c and d), which matches precisely with the microstructural analysis (Figs. 6a and b). The content of Ni ions in Li layer (Ni_{3a}) for both CS-750 and LNMO-800 cathodes as a function of charging voltage is shown in Fig. S23. Upon the first de-lithiation, the concentration of Ni_{3a} for both materials firstly decreases and reaches the minimum value in the high-voltage region (4.3–4.5 V), and increases suddenly with further charging to 4.6 V, which are consistent with the SXRD analysis (Figs. 5b, d) and previous results in the literature [59,60]. The content of Ni_{3a} in a deeply delithiated state (4.6 V) is approximately 5% for both cathodes. Therefore, the increased microstrain of Ni-rich cathodes along [003] direction is supposed to be dominantly linked to lattice distortion rather than the Li/Ni antisite defects.

With the online differential electrochemical mass spectrometry (DEMS) technique it is possible to detect various gasses in the electrolyte/electrode interfacial reaction products that are evolved during electrochemical cycling. As shown in Figs. 7(a) and (d), almost no O_2 gas is probed in both Li/CS-750 and Li/LNMO-800 cells. The CO_2 emission becomes obvious when the cells are charged above 4.0 V and reaches a maximum value of 362 nmol min ^{1} g ^{1} for Li/CS-750 cell and 1032 nmol min ^{1} g ^{1} for Li/LNMO-800 cell at the end of the first charge process (4.6 V). The overall CO_2 generation of Li/CS-750 cell is decreased by around 35% when compared with the Li/LNMO-800 cell.

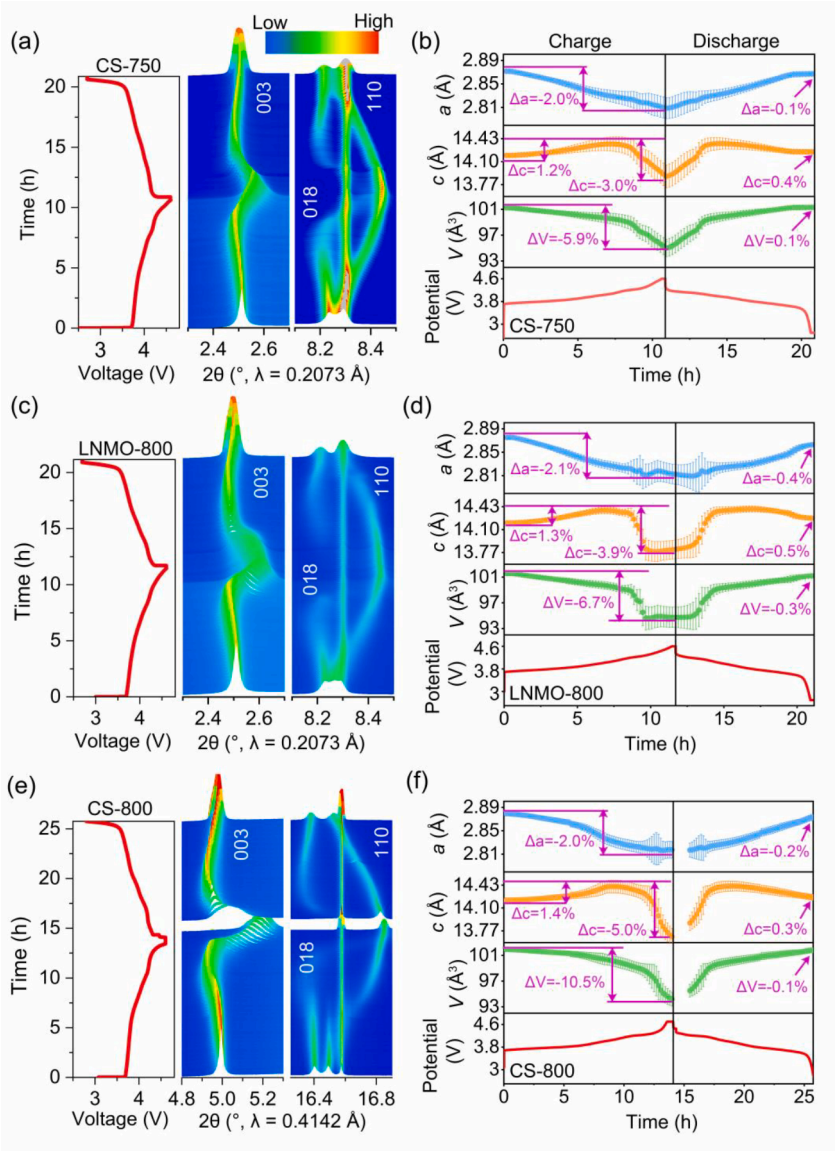

Fig. 5. Crystallographic changes of CS-750, LNMO-800 and CS-800 cathodes during the initial cycle in a voltage range of 2.7–4.6 V at 0.1 C. Three-dimensional (3D) maps of the intensity and position of 003, 018 and 110 reflections for (a) CS-750, (c) LNMO-800 and (e) CS-800 cathodes upon the first electrochemical cycle; the variations of lattice parameters and unit-cell volume of (b) CS-750, (d) LNMO-800 and (f) CS-800 electrodes as functions of reaction time.

These results suggest the core-shell architecture can effectively supress the lattice oxygen release and/or the decomposition of electrolyte during high-voltage cycling. In situ XAS experiments were also carried out to probe the oxidation state changes of Ni and Mn ions for both CS-750 and LNMO-800 electrodes during the first cycle, as shown in Figs. 7(b-c) and S24. Ni K-edge XANES spectra of CS-750 cathode collected at various states of charge/discharge exhibit a weak 1s → 3d pre-edge peak A, a shoulder peak B and an intense main absorption peak C (Fig. 7(b)). The main peak shifts towards higher energy during charge and then moves to lower energy during discharge, indicating the oxidation and reduction of Ni ions upon cycling (i.e. $Ni^{3+} \rightleftharpoons Ni^{4+} + e^{-}$). These results are in good accord with the contraction and expansion of lattice parameter *a* of the CS-750 electrode shown in Fig. 5(b). The Mn K-edge spectra of CS-750 cathode can be characterized by a doublet pre-edge peak A, a shoulder peak B, and a main absorption peak C (Fig. 7(c)). The intensity and position of pre-edge peak A and main peak C do not show obvious changes, revealing a very negligible change in the oxidation state of Mn ions during cycling. Peak B corresponding to ligand-to-metal charge transfer (LMCT) gradually vanishes, and peak B* progressively emerges during charging, which is correlated with changes in the electron density of the ligand. [61,62]

The Fourier transform (FT) magnitudes of k^2 weighted EXAFS spectra at Mn and Ni K-edges for CS-750 are plotted in Figs. 7(e, f). There are two distinct peaks in the FT spectra of two electrodes for Ni and Mn. The first peak at about 1.5 Å reflects the scattering interactions of TM-O, and the second one at approximately 2.5 Å corresponds to the TM-TM interactions. Interestingly, the intensity of Ni-O peak increases during delithiation and decreases during lithiation, indicating the changes in the degree of local structural disordering on Ni sites in the layered structure. The variations of XANES and EXAFS spectra of LNMO-800 are very similar to those of CS-750 electrode (see Fig. S24). The EXAFS fitting results of two electrodes are depicted in Figs. 7(g) and (h). Apparently, the average Ni-O bond distance ($d_{Ni\text{-}O}$) and the corresponding mean-square thermal displacement parameter ($\sigma^2_{Ni\text{-}O}$) of the electrodes shrink successively upon charging, revealing the oxidation of Ni ions and the reduction of local disorder on the Ni sites in the layered structure (and vice versa during discharging). The $d_{Mn\text{-}O}$ and $\sigma^2_{Mn\text{-}O}$ parameters of two samples stay nearly unchanged upon cycling, which suggest that the Mn

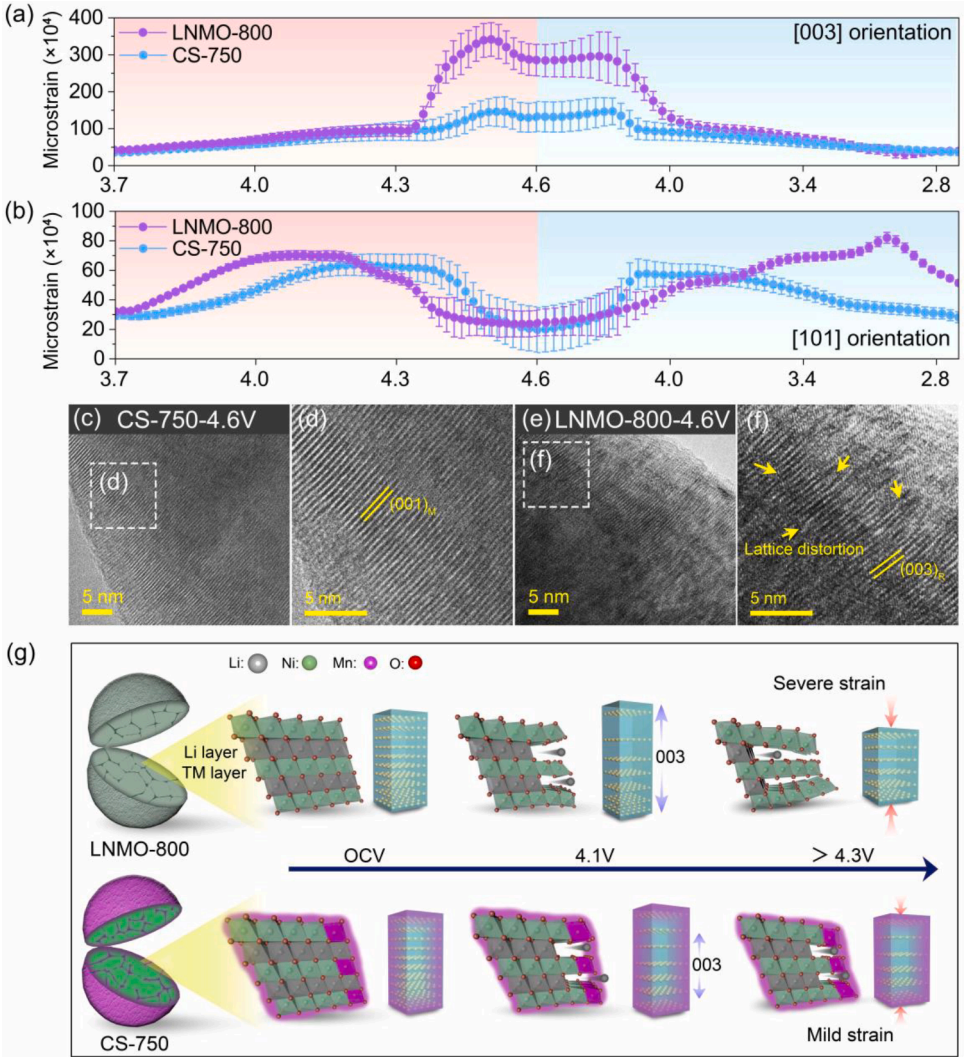

Fig. 6. Microstructural changes of CS-750 and LNMO-800 cathodes upon cycling. Lattice strain evolutions of CS-750 and LNMO-800 cathodes along (a) [003] and (b) [101] orientations as a function of reaction time. HRTEM images of (c, d) CS-750 and (e, f) LNMO-800 electrodes when charged to 4.6 V; (g) schematic illustration for the alleviation of the anisotropic microstrain in the layered structure upon de-lithiation process via introducing a Mn-rich outer surface.

ions do not participate in the redox reaction. It is worth noting that the $\sigma^2_{Ni\text{-}O}$ parameter of CS-750 is lower than that of LNMO-800 cathode in the state of charge (SoC) region of 50–85%, demonstrating that the degree of local structure disorder on Ni ions in the layered structure of CS-750 at high voltage is alleviated by introducing a core-shell architecture, which matches precisely with the analysis of in situ SXRD (Fig. 5) and ex situ HRTEM (Figs. 6c-f) images of these oxides.

After 100 cycles at 0.1C between 2.7 and 4.6 V, there are apparent lattice distortions at the surface of fatigued LNMO-800, as depicted in the HRTEM image (Fig. S25). Besides, two sets of spots from overlapping domains with two layered structures ($R\bar{3}m$) can be seen in the FFT patterns of cycled LNMO-800, which hint at the formation of an intermediate state during the transformation process from layered to spinel/rock-salt structure [15,39]. It is noted that the core-shell architecture of CS-750 is well maintained after prolonged cycling (see Figs. S26 and S27), confirming again the robust structural stability of core-shell architectured Ni-rich cathode materials upon high-voltage cycling. Moreover, a slight increase of cationic Li/Ni mixing is observed for both CS-750 and LNMO-800 after 100 cycles, as shown in Fig. S28. Ex situ XANES spectra at Ni and Mn K-edges shown in Fig. S29 illustrate that Ni valence state of two materials maintains a constant value (Ni^{2+}) after prolonged cycling. Comparably, the oxidation state of Mn ions is estimated to be approximately +3.8 for cycled CS-750 electrode and +3.6 for cycled LNMO-800 electrode, obtained by a linear combination fit (LCF) method. These results again prove an enhanced stability of lattice oxygen of "Li-rich Ni-rich" cathode materials with core-shell architecture during long-term cycling. Taken together, the core-shell architecture of Co-free Ni-rich layered cathode materials achieves the following two goals. First, the "Li-rich Ni-rich" core contributes to a high specific capacity. Meanwhile, the "Li-rich Mn-rich" shell can be regarded as a rivet, leading to the spontaneous formation of a mechanically stabilized structure (see Fig. 6g). Second, the lattice distortion and microstrain of Ni-rich cathode materials upon high-voltage cycling can be markedly suppressed by the less reactive monoclinic layered shell phase, resulting in mitigation of charge-transfer resistance growth during repeated lithiation/de-lithiation processes. Therefore, "Li-rich Ni-rich" oxides with such robust core-shell architecture could deliver enhanced chemo-mechanical stability and cyclic stability under high-voltage cycling conditions.

3. Conclusion

In summary, a two-step precipitation method followed by sintering with $LiOH{\bullet}H_2O$ was proposed to synthesize "Li-rich Ni-rich" core-shell $Li_{1.08}Ni_{0.9}Mn_{0.1}O_2$ cathode materials. The structural evolution and changes in the oxidation state of TM ions throughout the whole synthesis

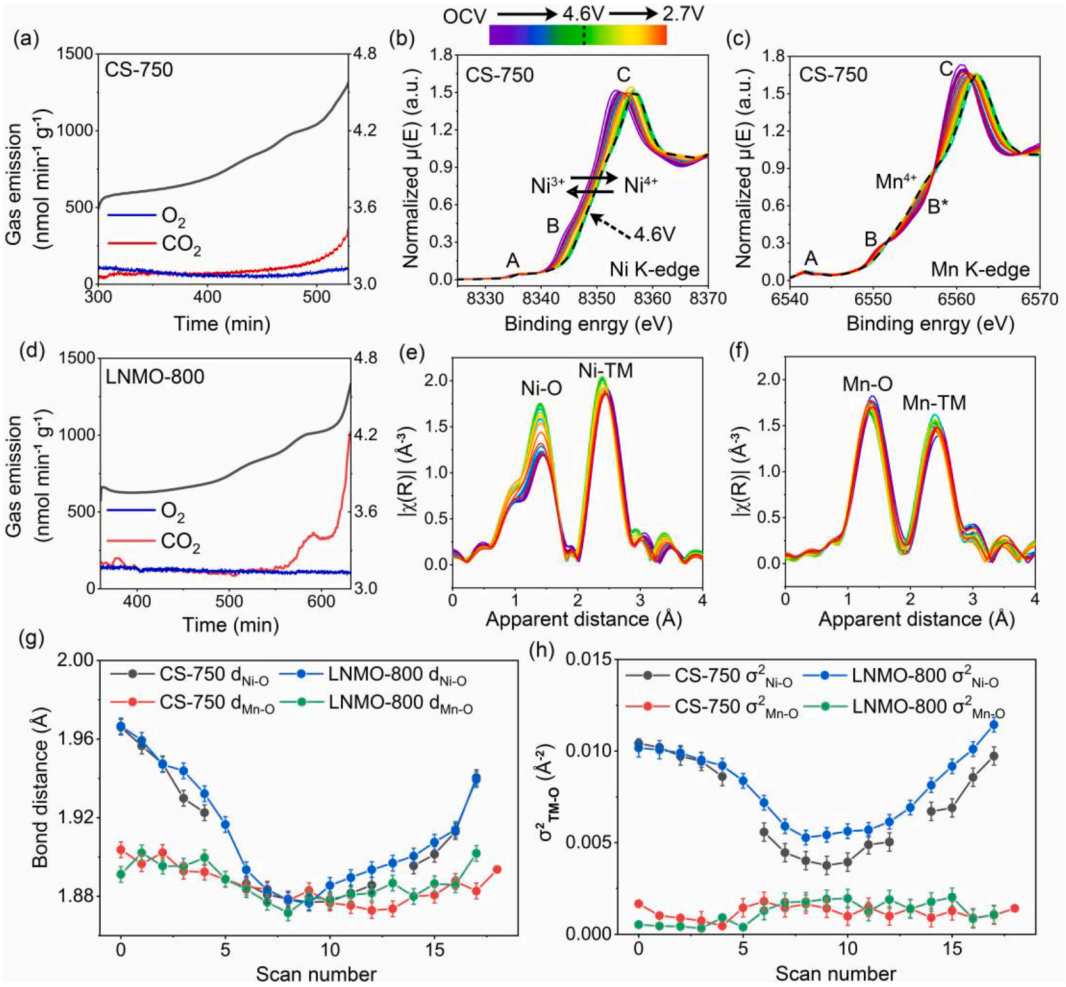

Fig. 7. DEMS measurements of gas evolution (i.e. O_2 and CO_2) on (a) a Li/CS750 cell and (d) a Li/LNMO-800 cell upon the first charge process; *in situ* XANES spectra at (b) Ni and (c) Mn K-edges of CS-750 cathode during the initial cycle; the Fourier transform magnitudes of k^2 weighted (e) Ni and (f) Mn K-edge EXAFS spectra for CS-750; variation of (g) bond distance and (h) mean-square thermal displacement parameters of Ni-O and Mn-O for both CS-750 and LNMO-800 cathodes upon the first cycle.

process were monitored to interpret the origin of cation interdiffusion caused by the concentration gradient. As lithium and oxygen gradually incorporate into the core-shell-architectured $Ni(OH)_2$@$Mn(OH)_2$ precursor, a "Li-rich Mn-rich" layered phase (*C2/m*) would be formed on top of a Ni-rich core ($R\bar{3}m$) during the high-temperature lithiation process. Such core-shell architecture can be well maintained within relatively lower heating temperatures (e.g. 650–700 °C). The "Li-rich Mn-rich" outer shell tends to become thinner and eventually disappears with increasing calcination temperature. In situ SXRD results demonstrate that the microstrain of "Li-rich Ni-rich" cathodes in the high-voltage regions could be suppressed effectively by the introduction of a "Li-rich Mn-rich" shell. With these peculiar benefits, the cycling stability of Ni-rich cathode materials with core-shell architecture has been demonstrated to be superior to materials with a uniform distribution of TM ions. Specifically, the CS-700 cathode exhibits a superior cyclability of about 79% after 500 cycles at 1 C during high-voltage cycling (4.6 V). Finally, these findings can broaden the prospects for designing and developing highly stable cathode materials for high-energy LIBs.

Supporting Information

Experimental sections, particle size distribution, TEM images, cross-sectional SEM images, SEM-EDX maps, ICP-MS results, *in situ /ex situ* SXRD patterns and XAS spectra, electrochemical impedance spectroscopy (EIS) spectra, Rietveld refinement results of SXRD data, crystallographic parameters and electrochemical performances of the samples.

CRediT authorship contribution statement

Zhiwei Jing: Investigation, Formal analysis, Writing – original draft. **Suning Wang:** Investigation, Formal analysis, Writing – review & editing. **Qiang Fu:** Investigation. **Volodymyr Baran:** Investigation. **Akhil Tayal:** Investigation. **Nicola P.M. Casati:** Investigation. **Alexander Missyul:** Investigation. **Laura Simonelli:** Investigation. **Michael Knapp:** Writing – review & editing. **Fujun Li:** Writing – review & editing. **Helmut Ehrenberg:** Methodology, Formal analysis, Writing – review & editing. **Sylvio Indris:** Methodology, Formal analysis, Writing – review & editing. **Chongxin Shan:** Writing – review & editing. **Weibo Hua:** Supervision, Formal analysis, Writing – original draft, Writing – review & editing.

Declaration of Competing Interest

The authors declare the following financial interests/personal relationships which may be considered as potential competing interests: Weibo Hua reports financial support was provided by National Natural Science Foundation of China.

Acknowledgments

This work was financially supported by the National Natural Science Foundation of China (Grant No. 22108218, 20A20145), the Guangxi Science and Technology Base and Talents Special Project (Grant No. AD21159007), the Natural Science Foundation of Guangxi (Grant No. 2020GXNSFBA297029), Distinguished Young Foundation of Sichuan Province (Grant No. 2020JDJQ0027) and Sichuan Province Science and Technology Achievement Transfer and Trans-formation Project (Grant No. 21ZHSF0111). W. H. acknowledges "Young Talent Support Plan" of Xi'an Jiaotong University and Qinchuangyuan Innovative Talent Project (QCYRCXM-2022–137). We acknowledge DESY (Hamburg, Germany), a member of the Helmholtz Association HGF, for the provision of experimental facilities. Parts of this research were carried out at P02.1, P64 and P65 beamlines. This work was performed by using the Biologic VMP-3 potentiostat of DESY/PETRA III beamline P02.1. Our research work has gained benefit from beamtime allocation at BL04-MSPD and BL22-CLAESS at ALBA Synchrotron, Barcelona, Spain. We also thank the Instrument Analysis Center of Xi'an Jiaotong University for the assistance test. This work contributes to the research performed at CELEST (Center for Electrochemical Energy Storage Ulm-Karlsruhe) and was supported by the German Research Foundation (DFG) under Project ID 390874152 (POLiS Cluster of Excellence).

References

[1] Y. Bi, J. Tao, Y. Wu, L. Li, Y. Xu, E. Hu, B. Wu, J. Hu, C. Wang, J.G. Zhang, Y. Qi, J. Xiao, Reversible planar gliding and microcracking in a single-crystalline Ni-rich cathode, Science 370 (2020) 1313–1317.

[2] T. Liu, J. Liu, L. Li, L. Yu, J. Diao, T. Zhou, S. Li, A. Dai, W. Zhao, S. Xu, Y. Ren, L. Wang, T. Wu, R. Qi, Y. Xiao, J. Zheng, W. Cha, R. Harder, I. Robinson, J. Wen, J. Lu, F. Pan, K. Amine, Origin of structural degradation in Li-rich layered oxide cathode, Nature 606 (2022) 305–312.

[3] A. Grenier, G.E. Kamm, Y. Li, H. Chung, Y.S. Meng, K.W. Chapman, Nanostructure transformation as a signature of oxygen redox in Li-rich 3d and 4d cathodes, J. Am. Chem. Soc. 143 (2021) 5763–5770.

[4] W. Hua, X. Yang, N.P.M. Casati, L. Liu, S. Wang, V. Baran, M. Knapp, H. Ehrenberg, S. Indris, Probing thermally-induced structural evolution during the synthesis of layered Li-, Na-, or K-containing 3d transition-metal oxides, eScience 2 (2022) 183–191.

[5] D. Rathore, M. Garayt, Y. Liu, C. Geng, M. Johnson, J.R. Dahn, C. Yang, Preventing interdiffusion during synthesis of Ni-rich core–shell cathode materials, ACS Energy Lett 7 (2022) 2189–2195.

[6] G.T. Park, H.H. Ryu, T.C. Noh, G.C. Kang, Y.K. Sun, Microstructure-optimized concentration-gradient NCM cathode for long-life Li-ion batteries, Mater. Today 52 (2022) 9–18.

[7] W. Hua, S. Wang, M. Knapp, S.J. Leake, A. Senyshyn, C. Richter, M. Yavuz, J. R. Binder, C.P. Grey, H. Ehrenberg, S. Indris, B. Schwarz, Structural insights into the formation and voltage degradation of lithium- and manganese-rich layered oxides, Nat. Commun. 10 (2019) 5365.

[8] W. Zhang, D.H. Seo, T. Chen, L. Wu, M. Topsakal, Y. Zhu, D. Lu, G. Ceder, F. Wang, Kinetic pathways of ionic transport in fast-charging lithium titanate, Science 367 (2020) 1030–1034.

[9] W. Zhang, Y. Li, L. Wu, Y. Duan, K. Kisslinger, C. Chen, D.C. Bock, F. Pan, Y. Zhu, A. C. Marschilok, E.S. Takeuchi, K.J. Takeuchi, F. Wang, Multi-electron transfer enabled by topotactic reaction in magnetite, Nat. Commun. 10 (2019) 1972.

[10] W. Zhang, H.C. Yu, L. Wu, H. Liu, A. Abdellahi, B. Qiu, J. Bai, B. Orvananos, F. C. Strobridge, X. Zhou, Z. Liu, G. Ceder, Y. Zhu, K. Thornton, C.P. Grey, F. Wang, Localized concentration reversal of lithium during intercalation into nanoparticles, Sci. Adv. 4 (2018) eaao2608.

[11] S. Tan, Z. Shadike, J. Li, X. Wang, Y. Yang, R. Lin, A. Cresce, J. Hu, A. Hunt, I. Waluyo, L. Ma, F. Monaco, P. Cloetens, J. Xiao, Y. Liu, X.Q. Yang, K. Xu, E. Hu, Additive engineering for robust interphases to stabilize high-Ni layered structures at ultra-high voltage of 4.8 V, Nat. Energy 7 (2022) 484–494.

[12] W. Hua, B. Schwarz, R. Azmi, M. Müller, M.S.D. Darma, M. Knapp, A. Senyshyn, M. Heere, A. Missyul, L. Simonelli, J.R. Binder, S. Indris, H. Ehrenberg, Lithium-ion (de)intercalation mechanism in core-shell layered Li(Ni,Co,Mn)O_2 cathode materials, Nano Energy 78 (2020), 105231.

[13] K. Märker, C. Xu, C.P. Grey, Operando NMR of NMC811/graphite lithium-ion batteries: structure, dynamics, and lithium metal deposition, J. Am. Chem. Soc. 142 (2020) 17447–17456.

[14] C. Xu, K. Märker, J. Lee, A. Mahadevegowda, P.J. Reeves, S.J. Day, M.F. Groh, S. P. Emge, C. Ducati, B.L. Mehdi, C.C. Tang, C.P. Grey, Bulk fatigue induced by surface reconstruction in layered Ni-rich cathodes for Li-ion batteries, Nat. Mater. 20 (2021) 84–92.

[15] W. Hua, J. Zhang, S. Wang, Y. Cheng, H. Li, J. Tseng, Z. Wu, C.H. Shen, O. Dolotko, H. Liu, S.F. Hung, W. Tang, M. Li, M. Knapp, H. Ehrenberg, S. Indris, X. Guo, Long-range cationic disordering induces two distinct degradation pathways in Co-free Ni-rich layered cathodes, Angew. Chem. Int. Ed. (2022), e202214880.

[16] L. Wang, T. Liu, T. Wu, J. Lu, Strain-retardant coherent perovskite phase stabilized Ni-rich cathode, Nature 611 (2022) 61–67.

[17] M.M. Thackeray, K. Amine, Layered Li–Ni–Mn–Co oxide cathodes, Nat. Energy 6 (9) (2021) 933.

[18] Y. Huang, H. Wei, P. Li, Y. Luo, Q. Wen, D. Le, Z. He, H. Wang, Y. Tang, C. Yan, K. Dai Mao, X. Zhang, J. Zheng, Enhancing structure and cycling stability of Ni-rich layered oxide cathodes at elevated temperatures via dual-function surface modification, J. Energy Chem. 75 (2022) 301–309.

[19] S. Lu, L. Tang, H. Wei, Y. Huang, C. Yan, Z. He, Y. Li, J. Mao, K. Dai, J. Zheng, Single-crystal nickel-based cathodes: fundamentals and recent advances, Electrochem. Energy Rev. 5 (2022) 15.

[20] Y. Luo, Q. Pan, H. Wei, Y. Huang, L. Tang, Z. Wang, Z. He, C. Yan, J. Mao, K. Dai, X. Zhang, J. Zheng, Towards Ni-rich layered oxides cathodes with low Li/Ni intermixing by mild molten-salt ion exchange for lithium-ion batteries, Nano Energy 102 (2022), 107626.

[21] U.H. Kim, G.T. Park, B.K. Son, G.W. Nam, J. Liu, L.Y. Kuo, P. Kaghazchi, C.S. Yoon, Y.K. Sun, Heuristic solution for achieving long-term cycle stability for Ni-rich layered cathodes at full depth of discharge, Nat. Energy 5 (2020) 860–869.

[22] W. Li, E.M. Erickson, A. Manthiram, High-nickel layered oxide cathodes for lithium-based automotive batteries, Nat. Energy 5 (2020) 26–34.

[23] X. Liu, G.L. Xu, V.S.C. Kolluru, C. Zhao, Q. Li, X. Zhou, Y. Liu, L. Yin, Z. Zhuo, A. Daali, J.J. Fan, W. Liu, Y. Ren, W. Xu, J. Deng, I. Hwang, D. Ren, X. Feng, C. Sun, L. Huang, T. Zhou, M. Du, Z. Chen, S.G. Sun, M.K.Y. Chan, W. Yang, M. Ouyang, K. Amine, Origin and regulation of oxygen redox instability in high-voltage battery cathodes, Nat. Energy 7 (2022) 808–817.

[24] J. Chen, Y. Yang, Y. Tang, Y. Wang, H. Li, X. Xiao, S. Wang, M.S.D. Darma, M. Etter, A. Missyul, A. Tayal, M. Knapp, H. Ehrenberg, S. Indris, W. Hua, Constructing a thin disordered self-protective layer on the $LiNiO_2$ primary particles against oxygen release, Adv. Funct. Mater. (2022), 2211515.

[25] L. Wang, X. Lei, T. Liu, A. Dai, D. Su, K. Amine, J. Lu, T. Wu, Regulation of surface defect chemistry toward stable Ni-rich cathodes, Adv. Mater. 34 (2022), e2200744.

[26] X.H. Meng, T. Lin, H. Mao, J.L. Shi, H. Sheng, Y.G. Zou, M. Fan, K. Jiang, R.J. Xiao, D. Xiao, L. Gu, L.J. Wan, Y.G. Guo, Kinetic origin of planar gliding in single-crystalline Ni-rich cathodes, J. Am. Chem. Soc. 144 (2022) 11338–11347.

[27] F. Wu, S. Fang, M. Kuenzel, A. Mullaliu, J.K. Kim, X. Gao, T. Diemant, G.T. Kim, S. Passerini, Dual-anion ionic liquid electrolyte enables stable Ni-rich cathodes in lithium-metal batteries, Joule 5 (2021) 2177–2194.

[28] H. Zhu, Y. Tang, K.M. Wiaderek, O.J. Borkiewicz, Y. Ren, J. Zhang, J. Ren, L. Fan, C.C. Li, D. Li, X.L. Wang, Q. Liu, Spontaneous strain buffer enables superior cycling stability in single-crystal nickel-rich NCM cathode, Nano Lett. 21 (2021) 9997–10005.

[29] J. Kim, H. Cho, H.Y. Jeong, H. Ma, J. Lee, J. Hwang, M. Park, Self-induced concentration gradient in nickel-rich cathodes by sacrificial polymeric bead clusters for high-energy lithium-ion batteries, Adv. Energy Mater. 7 (2017), 1602559.

[30] Y.K. Sun, S.T. Myung, M.H. Kim, J. Prakash, K. Amine, Synthesis and characterization of $Li[(Ni_{0.8}Co_{0.1}Mn_{0.1})_{0.8}(Ni_{0.5}Mn_{0.5})_{0.2}]O_2$ with the microscale core shell structure as the positive electrode material for lithium batteries, J. Am. Chem. Soc. 127 (2005) 13411–13418.

[31] Y.K. Sun, Z. Chen, H.J. Noh, D.J. Lee, H.G. Jung, Y. Ren, S. Wang, C.S. Yoon, S. T. Myung, K. Amine, Nanostructured high-energy cathode materials for advanced lithium batteries, Nat. Mater. 11 (2012) 942–947.

[32] N. Zhang, N. Zaker, H. Li, A. Liu, J. Inglis, L. Jing, J. Li, Y. Li, G.A. Botton, J. R. Dahn, Cobalt-free nickel-rich positive electrode materials with a core–shell structure, Chem. Mater. 31 (2019) 10150–10160.

[33] Y. Liu, D. Ouyang, D. Rathore, H. Wu, K. Li, Y. Wang, J. Sha, S. Yin, J.R. Dahn, An evaluation of a systematic series of cobalt-free Ni-rich core-shell materials as positive electrode materials for Li-ion batteries, J. Electrochem. Soc. 168 (9) (2021), 090555.

[34] L. Ni, R. Guo, S. Fang, J. Chen, J. Gao, Y. Mei, S. Zhang, W. Deng, G. Zou, H. Hou, X. Ji, Crack-free single-crystalline Co-free Ni-rich $LiNi_{0.95}Mn_{0.05}O_2$ layered cathode, eScience 2 (2022) 116–124.

[35] H. Zhang, Y. Yang, H. Xu, L. Wang, X. Lu, X. He, $Li_4Ti_5O_{12}$ spinel anode: fundamentals and advances in rechargeable batteries, InfoMat. 4 (2021) e12228.

[36] B. Li, G. Rousse, L. Zhang, M. Avdeev, M. Deschamps, A. Abakumov, J.M. Tarascon, Constructing "Li-rich Ni-rich" oxide cathodes for high-energy-density Li-ion batteries, Energy Environ. Sci. 16 (2023) 1210–1222.

[37] T. Zhou, H. Wang, Y. Wang, P. Jiao, Z. Hao, K. Zhang, J. Xu, J.B. Liu, Y.S. He, Y. X. Zhang, L. Chen, L. Li, W. Zhang, Z.F. Ma, J. Chen, Stabilizing lattice oxygen in slightly Li-enriched nickel oxide cathodes toward high-energy batteries, Chem 8 (2022) 2817–2830.

[38] Z. Cheng, B. Zhao, Y.J. Guo, L. Yu, B. Yuan, W. Hua, Y.X. Yin, S. Xu, B. Xiao, X. Han, P.F. Wang, Y.G. Guo, Mitigating the large-volume phase transition of P2-type cathodes by synergetic effect of multiple ions for improved sodium-ion batteries, Adv. Energy Mater. 12 (2022), 2103461.

[39] W. Hua, M. Chen, B. Schwarz, M. Knapp, M. Bruns, J. Barthel, X. Yang, F. Sigel, R. Azmi, A. Senyshyn, A. Missiul, L. Simonelli, M. Etter, S. Wang, X. Mu, A. Fiedler, J.R. Binder, X. Guo, S. Chou, B. Zhong, S. Indris, H. Ehrenberg, Lithium/oxygen

incorporation and microstructural evolution during synthesis of Li-rich layered Li$[Li_{0.2}Ni_{0.2}Mn_{0.6}]O_2$ oxides, Adv. Energy Mater. 9 (8) (2019), 1803094.
[40] W. Hua, Z. Wu, M. Chen, M. Knapp, X. Guo, S. Indris, J.R. Binder, N.N. Bramnik, B. Zhong, H. Guo, S. Chou, Y.M. Kang, H. Ehrenberg, Shape-controlled synthesis of hierarchically layered lithium transition-metal oxide cathode materials by shear exfoliation in continuous stirred-tank reactors, J. Mater. Chem. A 5 (2017) 25391–25400.
[41] S. Wang, W. Hua, A. Missyul, M.S.D. Darma, A. Tayal, S. Indris, H. Ehrenberg, L. Liu, M. Knapp, Kinetic control of long-range cationic ordering in the synthesis of layered ni-rich oxides, Adv. Funct. Mater. (2021) 31.
[42] W. Hua, W. Liu, M. Chen, S. Indris, Z. Zheng, X. Guo, M. Bruns, T.H. Wu, Y. Chen, B. Zhong, S. Chou, Y.M. Kang, H. Ehrenberg, Unravelling the growth mechanism of hierarchically structured $Ni_{1/3}Co_{1/3}Mn_{1/3}(OH)_2$ and their application as precursors for high-power cathode materials, Electrochim. Acta 232 (2017) 123–131.
[43] H. Yu, Y. Cao, L. Chen, Y. Hu, X. Duan, S. Dai, C. Li, H. Jiang, Surface enrichment and diffusion enabling gradient-doping and coating of Ni-rich cathode toward Li-ion batteries, Nat. Commun. 12 (2021) 4564.
[44] H.H. Sun, U.H. Kim, J.H. Park, S.W. Park, D.H. Seo, A. Heller, C.B. Mullins, C. S. Yoon, Y.K. Sun, Transition metal-doped Ni-rich layered cathode materials for durable Li-ion batteries, Nat. Commun. 12 (2021) 6552.
[45] L. Qiu, Y. Song, M. Zhang, Y. Liu, Z. Yang, Z. Wu, H. Zhang, W. Xiang, Y. Liu, G. Wang, Y. Sun, J. Zhang, B. Zhang, X. Guo, Structural reconstruction driven by oxygen vacancies in layered Ni-rich cathodes, Adv. Energy Mater. 12 (11) (2022), 2200022.
[46] W. Lee, S. Muhammad, T. Kim, H. Kim, E. Lee, M. Jeong, S. Son, J.H. Ryou, W. S. Yoon, New insight into Ni-rich layered structure for next-generation Li rechargeable batteries, Adv. Energy Mater. 8 (4) (2018), 1701788.
[47] J. Zhang, Q. Zhang, D. Wong, N. Zhang, G. Ren, L. Gu, C. Schulz, L. He, Y. Yu, X. Liu, Addressing voltage decay in Li-rich cathodes by broadening the gap between metallic and anionic bands, Nat. Commun. 12 (2021) 3071.
[48] Y. Yu, P. Karayaylali, S.H. Nowak, L. Giordano, M. Gauthier, W. Hong, R. Kou, Q. Li, J. Vinson, T. Kroll, D. Sokaras, C.J. Sun, N. Charles, F. Maglia, R. Jung, Y. Shao-Horn, Revealing electronic signature of lattice oxygen redox in lithium ruthenates and implications for high-energy Li-ion battery material designs, Chem. Mater. 31 (2019) 31.
[49] J. Rana, M. Stan, R. Kloepsch, J. Li, G. Schumacher, E. Welter, I. Zizak, J. Banhart, M. Winter, Structural changes in Li_2MnO_3 cathode material for Li-ion batteries, Adv. Energy Mater. 4 (2014), 1300998.
[50] M.M. Thackeray, S.H. Kang, C.S. Johnson, J.T. Vaughey, R. Benedek, S.A. Hackney, Li_2MnO_3-stabilized $LiMO_2$ (M = Mn, Ni, Co) electrodes for lithium-ion batteries, J. Mater. Chem. 17 (30) (2007) 3112–3125.
[51] J.Y. Liao, S.M. Oh, A. Manthiram, Core/double-shell type gradient Ni-rich $LiNi_{0.76}Co_{0.10}Mn_{0.14}O_2$ with high capacity and long cycle life for lithium-ion batteries, ACS Appl. Mater. Interfaces 8 (2016) 24543–24549.
[52] H.H. Sun, J.A. Weeks, A. Heller, C.B. Mullins, Nanorod gradient cathode: preventing electrolyte penetration into cathode particles, ACS Appl. Energy Mater. 2 (2019) 6002–6011.
[53] U.H. Kim, J.H. Kim, J.Y. Hwang, H.H. Ryu, C.S. Yoon, Y.K. Sun, Compositionally and structurally redesigned high-energy Ni-rich layered cathode for next-generation lithium batteries, Mater. Today 23 (2019) 26–36.
[54] T. Liu, L. Yu, J. Lu, T. Zhou, X. Huang, Z. Cai, A. Dai, J. Gim, Y. Ren, X. Xiao, M. V. Holt, Y.S. Chu, I. Arslan, J. Wen, K. Amine, Rational design of mechanically robust Ni-rich cathode materials via concentration gradient strategy, Nat. Commun. 12 (1) (2021) 6024.
[55] C. Zhang, T. Li, B. Xue, X. Wu, L. Li, Y. Guo, L. Zhang, Synergistic modification of Ni-rich full concentration gradient materials with enhanced thermal stability, Chem. Eng. J. 451 (2023), 138518.
[56] U.H. Kim, H.H. Ryu, J.H. Kim, R. Mücke, P. Kaghazchi, C.S. Yoon, Y.K. Sun, Microstructure-controlled Ni-rich cathode material by microscale compositional partition for next-generation electric vehicles, Adv. Energy Mater. 9 (15) (2019), 1803902.
[57] C. Xu, P.J. Reeves, Q. Jacquet, C.P. Grey, Phase behavior during electrochemical cycling of Ni-rich cathode materials for Li-ion batteries, Adv. Energy Mater. 11 (2021), 2003404.
[58] H. Wei, L. Tang, Y. Huang, Z. Wang, Y. Luo, Z. He, C. Yan, J. Mao, K. Dai, J. Zheng, Comprehensive understanding of Li/Ni intermixing in layered transition metal oxides, Mater. Today 51 (2021) 365–392.
[59] Q. Wang, C. Shen, S. Shen, Y. Xu, C. Shi, L. Huang, J. Li, S. Sun, Origin of structural evolution in capacity degradation for overcharged NMC622 via operando coupled investigation, ACS. Appl. Mater. Interfaces 9 (2017) 24731–24742.
[60] C. Shen, Q. Wang, H. Chen, C. Shi, H. Zhang, L. Huang, J. Li, S. Sun, *In situ* multitechnical investigation into capacity fading of high-voltage $LiNi_{0.5}Co_{0.2}Mn_{0.3}O_2$, ACS. Appl. Mater. Interfaces 8 (2016) 35323–35335.
[61] D. Dixon, S. Mangold, M. Knapp, H. Ehrenberg, A. Bhaskar, Direct observation of reductive coupling mechanism between oxygen and iron/nickel in cobalt-free Li-Rich cathode material: an in operando X-ray absorption spectroscopy study, Adv. Energy Mater. 11 (2021), 2100479.
[62] K. Okamoto, K. Shizuka, T. Akai, Y. Tamaki, K. Okahara, M. Nomura, X-ray absorption fine structure study on layered $LiMO_2$ (M = Ni , Mn , Co) Cathode materials, J. Electrochem. Soc. 153 (2006) A1120.